



Modification of NMC811 with titanium for enhanced cycling and high-voltage stability

Francesco Bizzotto, Walid Dachraoui, Rabeb Grissa, Wengao Zhao, Francesco Pagani, Edouard Querel, Ruben-Simon Kühnel*, Corsin Battaglia

Empa – Swiss Federal Laboratories for Materials Science and Technology, Dübendorf 8600, Switzerland

ARTICLE INFO

Keywords:

Nickel-rich NMC
TiO₂
Cathode
High voltage
Lithium-ion battery

ABSTRACT

LiNi_{1-x-y}Mn_xCo_yO₂ (NMC) with a nickel content of $\geq 80\%$ is currently considered one of the most promising lithium-ion battery cathode materials for applications that require both a high energy density and reasonable costs. However, its widespread use has so far been limited by its inherently lower structural stability and higher surface reactivity compared to NMC materials with a lower nickel content. Here, we explore wet-chemical titanium-based bulk and surface modifications to improve the cycling and high-voltage stability of NMC811. We find that both doping and coating with titanium improve cycling stability. For example, the capacity retention of graphite/NMC811 full cells cycled for 200 cycles between 2.8 and 4.4 V at C/3 improves from 86.1% for the pristine NMC811 to 89.4% and 91.5% for the doped and coated samples, respectively. Combining doping and coating in a two-step process results in a material with the most balanced properties in terms of capacity, cycling stability, rate performance, and high-voltage stability.

1. Introduction

Nickel-rich LiNi_{1-x-y}Mn_xCo_yO₂ (NMC, $1-x-y \geq 0.8$) is currently considered one of the most promising cathode materials for high-energy-density lithium-ion batteries for mobility applications. With increasing nickel content, degradation mechanisms become more pronounced limiting the long-term cycling stability in a battery cell especially when cycling to cell voltages > 4.2 V. Degradation mechanisms include the cracking of NMC particles due to anisotropic volume changes upon continuous charge and discharge and formation of a cation-disordered spinel phase (space group Fd3m) at the surface of the primary particles of nickel-rich NMC upon continuous cycling due to cation mixing [1–3]. This spinel phase subsequently transforms into an insulating cation-disordered rock salt phase (space group Fm3m). During this process, there is charge transfer from O²⁻ to the transition metals with release of oxygen that can react with the electrolyte leading to an increased interfacial resistance of the electrode resulting from electrolyte decomposition products. Nickel-rich NMC materials are also characterized by high sensitivity to air and moisture that lead to the formation of LiOH and Li₂CO₃ on the surface [4]. These compounds are responsible for gas formation during battery cycling and gelation of the slurry during electrode preparation [5].

Several attempts have been made to mitigate degradation of nickel-rich NMC. One approach involves the incorporation of dopants that strengthen the transition metal (TM)-oxygen bonds to reduce oxygen release. Moreover, metal dopants can provide charge compensation which balances the electrostatic repulsion between oxygen atoms and reduces Li/Ni mixing [6]. The range of dopants that have been proposed is quite broad and includes Al, Mg, Ti, Cr, Ga, Mo, W, Ta and Nb. The dopant can be introduced during the co-precipitation step of the Ni_{1-x-y}Mn_xCo_y(OH)₂ hydroxide precursor or during the subsequent high-temperature solid-state reaction to LiNi_{1-x-y}Mn_xCo_yO₂ [6,7]. Co-doping with two dopants has also been proposed [8].

Another strategy that has been widely employed is the modification of the surface of NMC particles by addition of a protective particle coating that reduces the reactivity towards the electrolyte at high voltage. Such coatings can be insulating metal oxides such as Al₂O₃, TiO₂, or ZrO₂. However, such coatings tend to negatively affect the cell's rate capability and therefore should have a thickness of only a few nanometers. Lithium-ion conductors such as LiNbO₃, Li₂SiO₃, or Li₂ZrO₃ have also shown promise due to their stability and reduced effect on the cell's rate capability [9–11]. The synthesis of the coating is usually performed by means of wet or solid-state chemistry or atomic layer deposition (ALD) [12]. The former methods have the advantage of being

* Corresponding author.

E-mail address: ruben-simon.kuehnel@empa.ch (R.-S. Kühnel).

<https://doi.org/10.1016/j.electacta.2023.142758>

Received 26 September 2022; Received in revised form 26 May 2023; Accepted 19 June 2023

Available online 20 June 2023

0013-4686/© 2023 The Authors. Published by Elsevier Ltd. This is an open access article under the CC BY license (<http://creativecommons.org/licenses/by/4.0/>).

easier and less expensive to scale up, whereas ALD allows for a high level of control of thickness and composition of the coating [13].

Among the elements that have been employed to enhance the cycling stability, titanium (Ti) is particularly attractive because of the high Ti-O bond strength as well as titanium's abundance and relatively low cost [14]. In previous studies, Fan *et al.* showed that a TiO₂ coating improves the cycling stability of NMC811 by minimizing contact between the active material and the electrolyte [15]. Furthermore, Wang *et al.* showed that TiO₂ reduces the air and moisture sensitivity of NMC622 [16].

Here, we systematically compare the effects of Ti doping and TiO₂ coating of NMC811 particles on cycling stability and rate capability. Moreover, we combine doping and coating in a two-step process in which NMC811 is first selectively doped with Ti and then coated with TiO₂. We compare the changes in NMC811 crystal structure, surface morphology, and composition as well as electrochemical properties upon these modifications.

2. Experimental

2.1. Synthesis of NMC811

Ni_{0.8}Mn_{0.1}Co_{0.1}(OH)₂ was synthesized by co-precipitation in a continuously stirred tank reactor under N₂ atmosphere. 1 L of distilled water was filled in a 3 L reactor followed by continuous injection of a total of one mole of transition metals into the reactor using 2 M aqueous solutions of NiSO₄, CoSO₄, and MnSO₄ in a ratio of 8:1:1. The injection rate was set to 1.5 ml/min. Meanwhile, 1 M NH₃·H₂O and 2 M NaOH were fed into the reactor as chelating and precipitation agent, respectively. During and 2 h after injection of the sulfate solutions, the vessel was continuously stirred at 750 rpm while maintaining a constant pH of 11.2 and a temperature of 50 °C. The Ni_{0.8}Mn_{0.1}Co_{0.1}(OH)₂ precursor was then filtered and washed several times with distilled water, and subsequently dried at 120 °C overnight. LiNi_{0.8}Mn_{0.1}Co_{0.1}O₂ was obtained by mixing the Ni_{0.8}Mn_{0.1}Co_{0.1}(OH)₂ precursor with LiOH·H₂O with a Li/transition metal ratio of 1.03. The LiOH·H₂O was previously ball milled to a fine powder in a planetary mixer with 10 mm stainless steel balls for 15 min at 650 rpm. The Ni_{0.8}Mn_{0.1}Co_{0.1}(OH)₂ precursor and the finely milled LiOH·H₂O were extensively mixed in the planetary mixer for 15 min at 150 rpm using 5 mm stainless steel balls. The Ni_{0.8}Mn_{0.1}Co_{0.1}(OH)₂/LiOH·H₂O mixture was then preheated at 500 °C for 10 h, cooled down to room temperature, and finally calcined at 750 °C for 15 h in a tube furnace in pure oxygen at a flow rate of 110 mL/min. Between the two calcination steps, the powder was gently milled in the planetary mixer with 5 mm stainless steel balls for 5 min at 150 rpm.

2.2. Modification of NMC811

The modifications of NMC811 were performed inside an argon-filled glovebox by adding freshly calcined NMC811 to the solution of the coating/doping precursor. In a typical synthesis, 5 g of NMC811 were dispersed in 4 mL of a solution of titanium ethoxide (Ti(OEt)₄) (Sigma Aldrich, ≤ 3% tetraisopropyl orthotitanate) in absolute ethanol (Sigma Aldrich, 99.8 %) pre-dried with molecular sieves. The amount of Ti (OEt)₄ was carefully adjusted based on the exact weight of NMC811 to be coated. A typical concentration was ca. 75 μmol_{Ti}/mL_{EtOH}. The 50 mL round-bottom flask was then sealed, removed from the glovebox, and sonicated for 5 min in a sonication bath to obtain a homogeneous dispersion. Subsequently, the ethanol was removed in a rotary evaporator. The round-bottom flask attached to the rotary evaporator was immersed in a sonication bath for 90 min at a rotation rate of 140 rpm while the pressure was reduced to 600 mbar. The pressure was then reduced to 120 mbar to evaporate the ethanol and finally to 10 mbar to remove the remaining ethanol. The powder was then collected and gently ball-milled for 5 min inside a 15 mL stainless steel jar containing 5 mm steel balls to obtain a fine and homogeneous powder. The powder

was then transferred into an alumina crucible and calcined for 5 h in a tube furnace in pure oxygen at a flow rate of 60 mL/min. Three samples, labeled NMC-C, NMC-D, NMC-D-C, were prepared using different calcination protocols that are summarized in Table 1. As-synthesized pristine NMC-P is used as a reference.

The powders were then sieved to remove agglomerates larger than 50 μm and stored inside an argon-filled glovebox for further use.

2.3. Transmission and scanning electron microscopy

Cross-sectional specimens for electron microscopy were prepared using the focused ion beam (FIB) of a FEI Helios Nanolab 660 FIB/SEM operated at acceleration voltages of 30 and 5 kV. The sample preparation can be summarized into the following steps: depositing protective layers, digging pits, extracting the sample, welding the sample on OMNI probe Cu grid, and thinning. High-angle annular dark-field (HAADF) scanning transmission electron microscopy (STEM) images and energy dispersive spectroscopy (EDS) elemental mapping were carried out using an FEI Titan Themis 80–300 STEM with a probe Cs-corrector operated at 300 kV. The HAADF-STEM images were processed using ImageJ and Gatan DigitalMicrograph. Scanning electron microscopy (SEM) images were acquired using a Hitachi S-4800. Selected electrodes were ion-milled for 2 h at -70 °C using the broad ion beam of a Hitachi IM4000Plus and coated with 5 nm of carbon before images were taken.

2.4. X-ray diffraction

Powder X-ray diffraction (XRD) measurements were performed on fresh and electrochemically aged NMC powder. All experiments involving electrodes were carried out in a spinning capillary configuration on a Malvern Panalytical Empyrean X-ray diffractometer equipped with a Cu-Kα radiation source. All samples were gently ground with mortar and pestle before loading the fine powder into a glass capillary that was subsequently sealed. The electrodes used for electrochemistry were also rinsed with dimethyl carbonate (DMC) before putting them in the mortar. Data collection was performed in the 2θ range of 10 – 90° with a step interval of 0.008° and a step time of 700 s. Rietveld refinement analysis was performed using the FullProf software. Thompson-Cox-Hastings pseudo-Voigt function was employed as a peak shape function [17]. The freshly synthesized NMC powders were instead analyzed using flat sample holders in reflection mode on a Panalytical X'pert PRO X-ray diffractometer equipped with a Cu-Kα radiation source. For the refinement, the isotropic displacement parameter (Biso) was kept constant at 1 for all sites for the fresh powder measured in flat sample configuration, whereas it was decreased to 0.5 for the samples measured with the spinning capillary. We refined the scale factor, the site occupancy, and the lattice parameters. All measurements were conducted at room temperature.

2.5. Electrode fabrication and battery assembly

Freshly synthesized and sieved NMC powder was gently mixed in a mortar with carbon black (Super C65, Imerys). The powder was then quantitatively transferred to a stainless steel bowl with a solution of PVdF (Solef 5130, Solvay) in *N*-methyl-2-pyrrolidone (Sigma Aldrich,

Table 1

Sample acronym, modification approach, amount of Ti, and annealing conditions used in the preparation of the three modified NMC811 samples.

Sample	Modification	Ti [mol.%]	Annealing conditions
NMC-C	Coating	0.6	500 °C, 5 h, O ₂
NMC-D	Doping	0.6	750 °C, 5 h, O ₂
NMC-D-C	Doping + Coating	0.3 (doping) + 0.6 (coating)	Doping: 750 °C, 5 h, O ₂ Coating: 500 °C, 5 h, O ₂

99.5 %) with a concentration of 33 mg_{PVdF}/mL_{NMP}. The mass ratio of NMC, carbon black and PVdF was 94:3:3. The bowl was then transferred to a planetary mixer that was run for 30 minutes, with cycles consisting of 2 minutes rotation at 650 rpm interrupted by 1 minute of rest. The homogeneous slurry was then tape cast on an Al foil. The electrodes were then dried for 2 h in air at 80 °C. Once the electrodes were dry, 12 and 14 mm discs were punched out and pressed at 1.5 t/cm² for 30 s. Each electrode was then weighed and dried for 12 h at 120 °C in vacuum (1·10⁻³ mbar) inside a glass oven. For full cells, we used graphite electrodes with a capacity of 2.8 mAh/cm² and a composition of 95 wt.% graphite (SMG-A5, Hitachi), 0.5 wt.% carbon black (Super C65, Imerys), 1.5 wt.% styrene-butadiene rubber (SBR, LIPATON SB 5521, Synthomer) and 3 wt.% sodium carboxymethyl cellulose (CMC, WALOCEL CRT 2000 PA, Dow Wolff Cellulosics).

Two-electrode cells were prepared with 2032 stainless steel coin cells. Celgard 2500 was used as separator and 35 µL of 1 M LiPF₆ in EC:EMC 3:7 by volume with 2 wt.% of VC (Solvionic) was employed as electrolyte. For full cells, one spacer with a thickness of 0.5 mm and one spacer with a thickness of 1 mm were employed. For half cells, only one spacer with a thickness of 1 mm was employed. In half cells, 12 mm positive electrodes with a capacity of ca. 1 mAh/cm² and a 14 mm lithium foil discs (99.9%, China Energy Lithium) with a thickness of 500 µm were used as electrodes. Full cells were assembled using 14 mm positive electrodes with a capacity of around 2.5 mAh/cm² and 15 mm graphite electrodes with a capacity of 2.8 mAh/cm², resulting in an N/P ratio of ca. 1.1. Cell assembly was carried out in an argon-filled glovebox. After assembly, the cells were rested in open-circuit condition for 12 h at 25 °C to ensure wetting of separator and electrodes.

2.6. Electrochemical protocols

For rate tests, 12 mm positive electrodes with a capacity of 1 mAh/cm² were utilized with lithium metal as the negative electrode. For each cell, we performed two formation cycles at C/10 followed by several steps where the charge rate was maintained at C/5 whereas the discharge rate was progressively increased from D/5 to 3D. All electrodes were cycled between 2.8 and 4.3 V vs. Li/Li⁺.

For the galvanostatic intermitted titration technique (GITT), after two formation cycles at C/10, we applied constant current steps of C/10 for 30 min followed by 4 h rest. This protocol was repeated until the cut-off voltage of 4.3 V was reached. The lithium diffusion coefficient was calculated with the model proposed by A. Nickol et al. [18]:

$$D_{Li} = \frac{4}{9\pi} \left(\frac{r_p}{t_p} \frac{E_4 - E_0}{dE/d\sqrt{t}} \right)^2 \quad (1)$$

where r_p is the radius of the NMC particles, t_p the duration of the current pulse, E_4 the voltage at the end of the rest, and E_0 the voltage before the start of the current pulse. Fig. S1 shows the evolution of the cell voltage during the GITT experiment. As can be seen in the inset of the figure, the voltage nearly stabilized after four hours of OCV. Fig. S2 is a typical example of the evolution of the cell voltage during the current pulses when plotted vs. the square root of time. As can be seen in the figure, we obtained good linearity at low states of charge (low cell voltages). However, the curves deviate from the expected linear behavior for higher states of charge (higher cell voltages), in line with the voltage profile of NMC (see, e.g., Fig. 4b). Hence, the diffusion coefficients reported in Fig. 3c for high states of charge are less reliable than the values reported for low states of charge.

For full cells, we used heavier 14 mm positive electrodes (2.5 mAh/cm²) and we performed three formation cycles at C/10 up to 4.2 or 4.4 V vs. graphite followed by continuous charge and discharge at C/3. All cycles included a constant current step followed by a constant voltage step (CCCV) at the upper cut-off voltage with a current threshold of C/20.

Accelerated aging tests (AATs) were performed in full cells after

three formation cycles at C/10 and two reference cycles at C/3. An example of the voltage and current profiles during the AAT can be found in Fig. S3. We carried out the AAT by driving the voltage at the constant rate of C/3 up to 4.2 V followed by a 10 h hold at this voltage. We then discharged the battery at C/3 down to 2.8 V before performing a full cycle with CCCV that we used to monitor the changes in specific capacity. To account for the excess of capacity obtained during the voltage hold with respect to a standard cycle with a CCCV protocol, we calculated a cumulative Coulombic efficiency (CCE) as:

$$CCE = \frac{\text{Discharge capacity}_{\text{Hold}} + \text{Discharge capacity}_{\text{Hold}+1}}{\text{Charge capacity}_{\text{Hold}} + \text{Charge capacity}_{\text{Hold}+1}} \quad (2)$$

Here, "Hold" refers to an accelerated aging cycle with the constant voltage step of 10 h and "Hold+1" refers to the next cycle, the standard CCCV cycle. Capacity retention was calculated by dividing the discharge capacity of the full cycles following the voltage hold by the discharge capacity of the second reference cycle performed after the formation cycles.

2.7. Thermal analysis

The thermal stability of charged NMC was investigated by means of differential scanning calorimetry (DSC), thermal gravimetric analysis (TGA), and mass spectrometry (MS) on a Netzsch STA 449 F3 Jupiter coupled to a Netzsch QMS 403 C mass spectrometer. A 2032 stainless steel coin cell was assembled with an NMC811 positive electrode with an active material loading of 12.5 mg/cm² and a lithium foil as negative electrode. Celgard 2500 was used as separator and 35 µL of 1 M LiPF₆ in EC:EMC 3:7 with 2 wt.% of VC (Solvionic) was employed as electrolyte. Cell assembly was carried out in an Ar-filled glovebox. After assembly, the cell was rested for 12 h at 25 °C to ensure wetting of separator and positive electrode. The cell was subsequently charged at C/10 up to 4.3 V followed by a constant voltage step at 4.3 V of 5 h. The cell was then disassembled in the charged state inside an argon-filled glove box. The positive electrode was recovered and thoroughly rinsed with DMC to remove the electrolyte residues. The electrode was maintained inside the glovebox for one hour to ensure the quantitative evaporation of the solvent. The active powder was then scratched from the Al current collector and transferred inside an Al crucible that was subsequently sealed. To allow release of gases, the crucible was pierced with a needle immediately before mounting the sample onto the sample holder of the STA to minimize contact with air. The chamber of the STA was then evacuated three times and a gas mixture with a composition of He:Ar=1.5:1 was flown over the sample throughout the thermal treatment. The sample was heated to 350 °C at a rate of 5 °C/min while simultaneously recording heat release/uptake and weight change, and tracking decomposition products via mass spectrometry.

2.8. X-ray photoelectron spectroscopy

X-ray photoelectron spectroscopy (XPS) measurements were performed at room temperature on a PHI Quantum 2000 using a monochromated Al K α X-ray source (1486.6 eV) and a pass energy of 30 eV. All measurements were conducted on three different areas, 150 µm in diameter, of each sample. Sample charging was prevented by charge compensation provided by a low-energy-electron and an argon-ion gun. XPS data were processed with the CasaXPS software and quantified using the corrected cross sections with the instrument parameters (Table S1). Spectra were calibrated by setting the hydrocarbon component of the C 1s photoemission peak to 285.0 eV binding energy. The samples were transferred from the glovebox to the XPS load lock under argon atmosphere using a home-built air tight transfer chamber.

3. Results and discussion

3.1. Morphology and composition of modified NMC811

As-synthesized pristine NMC811 (acronym NMC-P) was used as a baseline material and modified by mixing it with the titanium precursor $\text{Ti}(\text{OEt})_4$ and calcining the mixture at 500 or 750 °C. These temperatures were reported to typically yield coated and doped NMC, respectively [22,25]. Three materials were selected for this study: 1) NMC811 coated with 0.6 mol% of TiO_2 at 500 °C (acronym NMC-C), 2) NMC811 doped with 0.6 mol% of titanium at 750 °C (acronym NMC-D) and 3) NMC811 doped with 0.3 mol% titanium at 750 °C and subsequently coated with 0.6 mol % TiO_2 at 500 °C (acronym NMC-D-C). The mole percentages of Ti/TiO_2 are given relative to the transition metals of the NMC811 with n ($\text{Ni}+\text{Mn}+\text{Co}$) = 100%. A detailed description of these modifications can be found in Table 1 in the experimental section.

Fig. 1a–d compares the morphology of the pristine and titanium-modified NMC811 materials as observed by SEM. The shape of the particles does not appear to be affected by the titanium modification. For all samples, quasi-spherical secondary particles with a diameter of 10–15 μm are observed. Moreover, no agglomerates are visible at low magnification on the surface of the particles, suggesting a homogeneous distribution of titanium on the surface and no particle damage induced by the modification.

The effect of the titanium modification and the calcination becomes apparent at higher magnification. The primary particles of NMC-P (Fig. 1a) display sharp edges, whereas NMC-C and NMC-D-C (Fig. 1b and 1d) are characterized by less well-defined primary particles that hint

at the presence of a coating. Interestingly, the morphology of NMC-D (Fig. 1c) is nearly identical to that of NMC-P. At the higher calcination temperature of 750 °C (NMC-D) compared to 500 °C (NMC-C), the titanium seems to have diffused into the bulk of the NMC811 as discussed below.

Fig. 1e–h and 1i–l shows HAADF-STEM images of pristine and titanium-modified NMC samples and corresponding EDS maps, respectively. For NMC-C (Fig. 1j), the titanium is visibly more concentrated on the edge of the primary particle and forms a thin conformal layer with a thickness of around 5 nm. Such a continuous coating is absent for NMC-D (Fig. 1k). Instead, the titanium seems to be homogeneously dispersed over the entire material. This observation fits the SEM analysis and supports the expectation that titanium diffuses into the bulk of the material at high calcination temperatures. Similarly to NMC-C, a stronger titanium signal can be observed on the edges of the particles for NMC-D-C, indicating its accumulation on the surface.

All samples display an ordered layered structure which is clearly visible for NMC-P and NMC-D in the high-resolution HAADF-STEM images (Fig. S4), which do not exhibit a surface coating. For the coated samples, particularly for NMC-C, the layered structure is less clearly visible as it is masked by the coating (see again Fig. S4). However, both NMC-C and NMC-D-C display the electron diffraction pattern typical of the hexagonal R-3m phase of NMC (see insets in Fig. S4).

In Fig. 1k, no increased titanium concentration is measured near the surface, hinting that annealing at 750 °C allows titanium to diffuse into the bulk of NMC811. This hypothesis is supported by the cross-sectional STEM image of the freshly synthesized NMC-D where titanium appears uniformly distributed over the entire secondary particle (Fig. 2b). An

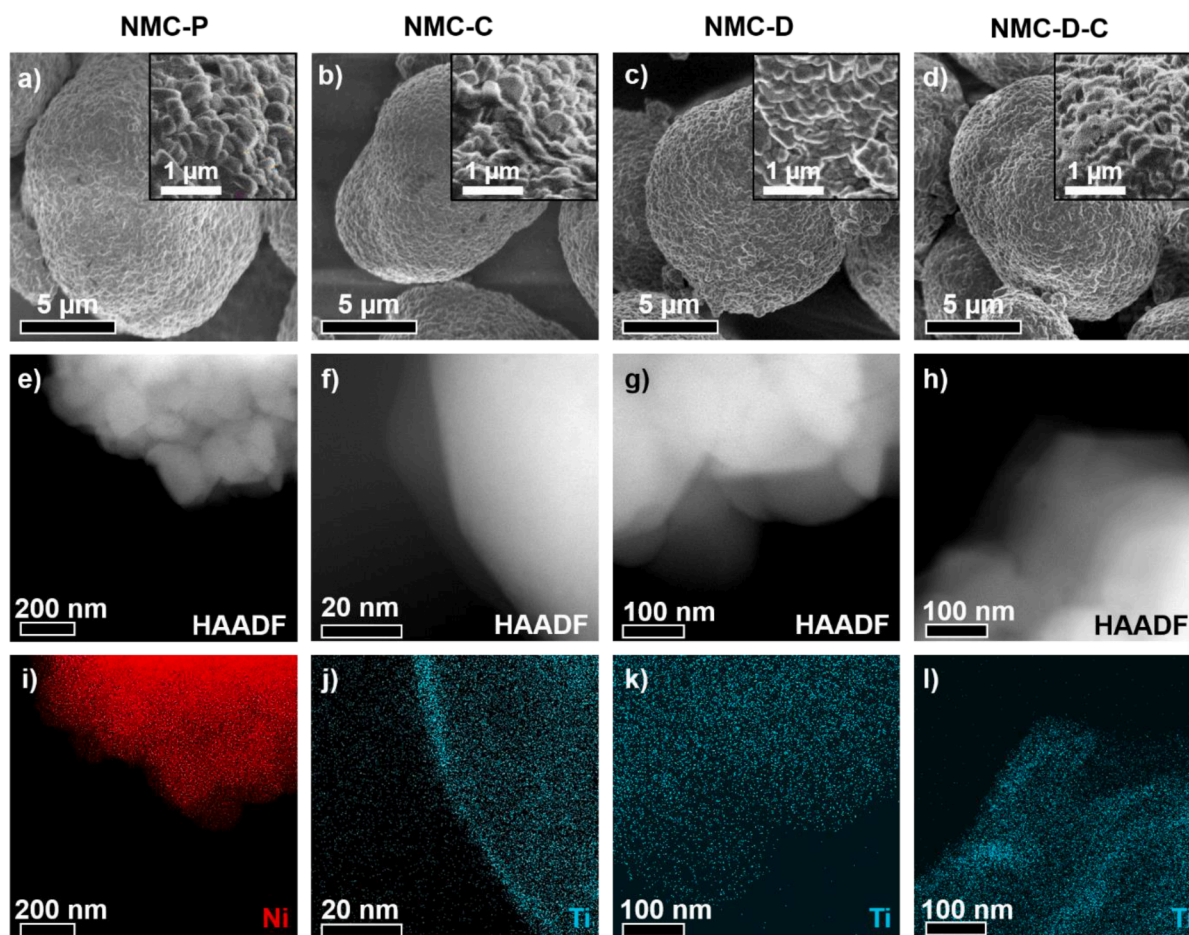


Fig. 1. Characterization of the as synthesized NMC powders with a–d) SEM, e–h) HAADF-STEM and i–l) EDS. All samples were coated with a carbon layer having a thickness of 3 nm before loading the sample into the electron microscopes.

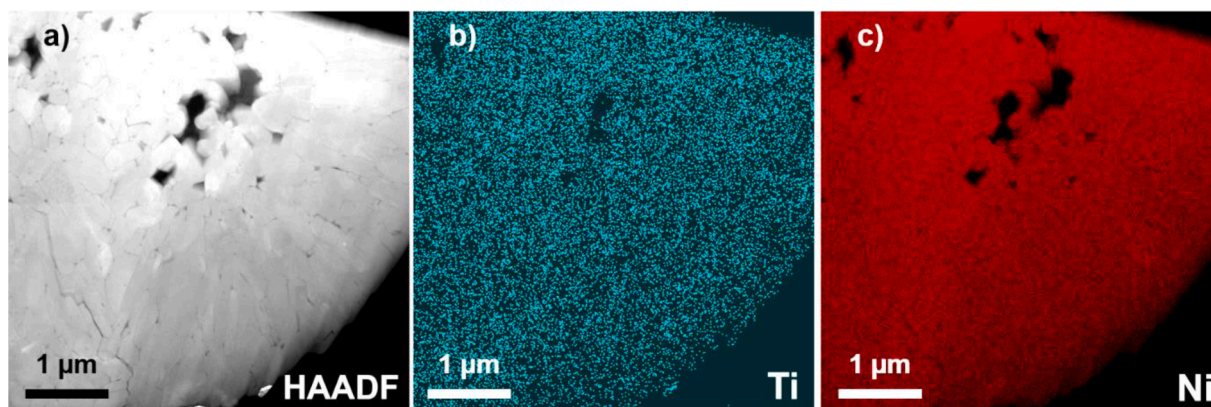


Fig. 2. Characterization of the freshly synthesized NMC-D powder by a) HAADF-STEM and b, c) EDS with the elemental distribution of b) Ti and c) Ni shown. The sample is a lamella prepared via focused ion beam.

inherent limitation of TEM is however the fact that it is a local technique. We therefore also investigated the NMC materials with XPS to obtain area-integrated information on their surface composition (Figs. S5 and S6). As expected, we find a lower amount of titanium relative to nickel (denoted as 'NMC' in the bars on the right side of Figs. S5 and S6) for NMC-D compared to NMC-C (Fig. S5). XPS is a surface sensitive technique which probes only the outermost atomic layers of the NMC secondary particles. From this observation, that is the average over a large portion of the electrodes, we can therefore confirm that the diffusion of titanium from the surface to the bulk takes place during annealing at 750 °C. At the same time, the XPS results confirm the presence of titanium on the surface for samples NMC-C and NMC-D-C, considering the visibly higher titanium-to-nickel ratio compared to sample NMC-D. Interestingly, we observed that the titanium-modified NMC materials also display a lower amount of residual lithium (LiOH and Li₂CO₃) relative to nickel on the surface with respect to NMC-P (Figs. S5 and S6), hinting at a lower moisture sensitivity.

3.2. Bulk crystal structure and thermal stability of modified NMC811

We refer to reference [19] for a discussion of the crystal structure of nickel-rich NMC. Table 2 reports the unit cell parameters, (003)/(104) peak intensity ratios, and the degree of cationic disorder, i.e., partial occupation of transition metal sites by lithium, of all samples determined via Rietveld refinement of the corresponding powder X-ray diffractograms (shown in Fig. S7). The unit cell dimensions are affected by the calcination temperature as well as by the amount of Ti. For a given amount of titanium employed during the coating/doping step, the unit cell size increases as a function of the calcination temperature. The *c*

lattice parameter of NMC-D is larger than that of NMC-C, which were annealed at 750 and 500 °C, respectively. Particularly for NMC-D, the *c* lattice parameter is significantly increased, suggesting at least partial replacement of transition metals by titanium in the structure of NMC, which is line with the larger size of Ti⁴⁺ (0.605 Å) compared to, e.g., Mn⁴⁺ (0.53 Å) [20]. Moreover, the lattice parameters are also affected by the amount of titanium employed. For NMC-D-C, the overall amount of titanium is 0.9 mol%, however, during the first calcination step at 750 °C which is responsible for the titanium diffusion into the structure we added only 0.3 mol% titanium resulting in a negligible change in the unit cell dimensions. The subsequent addition of titanium during the coating step did not yield the same larger unit cell recorded for NMC-D.

Besides an increase in the size of the unit cell, the degree of cationic disorder is also larger for all modified samples compared to NMC-P, which displays Ni/Li mixing of 2.0%. For the modified NMCs, the cationic disorder increases to values between 3.2 and 4.1% (Table 2). A higher annealing temperature during the modification process thus increases the degree of Ni/Li mixing. NMC-C and NMC-D were modified with the same amount of Ti, however, degrees of disorder of 4.0 and 3.7% were determined for NMC-D and NMC-C, respectively.

We also investigated the effect of the amount of titanium on Ni/Li mixing. Table 2 also reports data for an additional sample, NMC-D03, which was doped (i.e., annealed at 750 °C) with only 0.3 mol% titanium compared to 0.6% for NMC-D. For sample NMC-D03, we determined a value of 4.1%, indicating that the heat treatment is the main driving force for the increase in the degree of disorder and not the amount of Ti. In fact, it was reported in literature that a heat treatment above 400 °C increases Ni/Li disorder due to formation of oxygen vacancies [21]. The variations of the Ni/Li exchange also follow the same trend calculated for the (003)/(104) intensity ratios. This ratio is widely utilized to qualitatively estimate changes in the layered structure, with a larger ratio being representative of a more ordered material.

Thermal stability is of great importance as the threshold temperature for thermal runaway has been shown to decrease in cells with increasing nickel content in the NMC cathode [22]. We assess the thermal stability of positive electrodes charged to 4.3 V vs. Li by analyzing heat dissipation, mass loss, and oxygen release as a function of temperature (Fig. S8). We observe that NMC-D is characterized by the most significant increase in the decomposition temperature, i.e., from 225 °C for NMC-P to 235 °C for NMC-D. Moreover, from mass spectrometry we conclude that NMC-D displays the lowest oxygen release which may be attributed to the strong Ti-O bonds. The coated samples instead showed a smaller increase in the threshold temperature, i.e., 230 and 228 °C for NMC-C and NMC-D-C, respectively.

Table 2

Lattice parameters, (003)/(104) peak intensity ratios, and cationic disorder of the as synthesized NMC powders prepared for this study extracted from Rietveld refinements of the corresponding XRD patterns. The radiation employed was Cu Kα.

	<i>a</i> [Å]	<i>c</i> [Å]	<i>c/a</i>	<i>I</i> _{(003)/} <i>I</i> ₍₁₀₄₎ area	<i>I</i> _{(003)/} <i>I</i> ₍₁₀₄₎ height	Ni _{Li} [%]
NMC-P	2.8718 (1)	14.1993 (1)	4.9444 (1)	1.08	1.35	2.0(1)
NMC-C	2.8720 (1)	14.2081 (2)	4.9470 (3)	1.03	1.35	3.7(1)
NMC-D	2.8728 (1)	14.2108 (2)	4.9466 (3)	0.95	1.27	4.0(1)
NMC-D03	2.8724 (1)	14.1991 (1)	4.9433 (2)	0.90	1.13	4.1(1)
NMC-D-C	2.8730 (1)	14.1990 (2)	4.9421 (3)	1.00	1.27	3.2(1)

3.3. Electrochemical performance of modified NMC811

To study the rate performance of the different NMC811 samples, we carried out rate tests in half-cell configuration in which the discharge rate was varied between D/10 and 3D and the charge rate was not increased beyond C/5 (see experimental section for details). The pristine material (NMC-P) displays the highest specific capacity over the entire explored discharge rate range (Fig. 3a). In contrast, NMC-D has the lowest specific capacity at D/10 but displays the same capacity at 3D than NMC-P, i.e., a better capacity retention with increasing rate, which also manifests in a significantly lower discharge overpotential with respect to NMC-P (Fig. 3b). The lower initial capacity was ascribed previously to the increased degree of cationic disorder [23,24]. The improved rate performance instead can be ascribed to the larger unit cell of NMC-D compared to NMC-P. An increased c lattice parameter has

previously been reported as possible cause for faster bulk lithium diffusion in NMC considering that the activation barrier for lithium migration strongly depends on the lithium slab distance [25].

In contrast, the TiO_2 coating on NMC-C slightly reduces the rate performance, as previously reported for metal oxide coatings, although no increase in overpotential is visible in the voltage profiles at high discharge rates (Fig. 3b) [26]. However, even at a rate of 3D the specific capacity of NMC-C is only 4 mAh/g lower than that of NMC-P. We attribute this rather minor capacity loss to the small thickness of the coating of only a few nanometers.

NMC-D-C, that has been doped and coated, shows an intermediate behavior between NMC-D and NMC-C in terms of rate performance. It benefits from lower cationic disorder compared to NMC-D but not from an increased c lattice parameter relative to NMC-P. Moreover, the presence of the coating layer is also expected to slightly hinder lithium

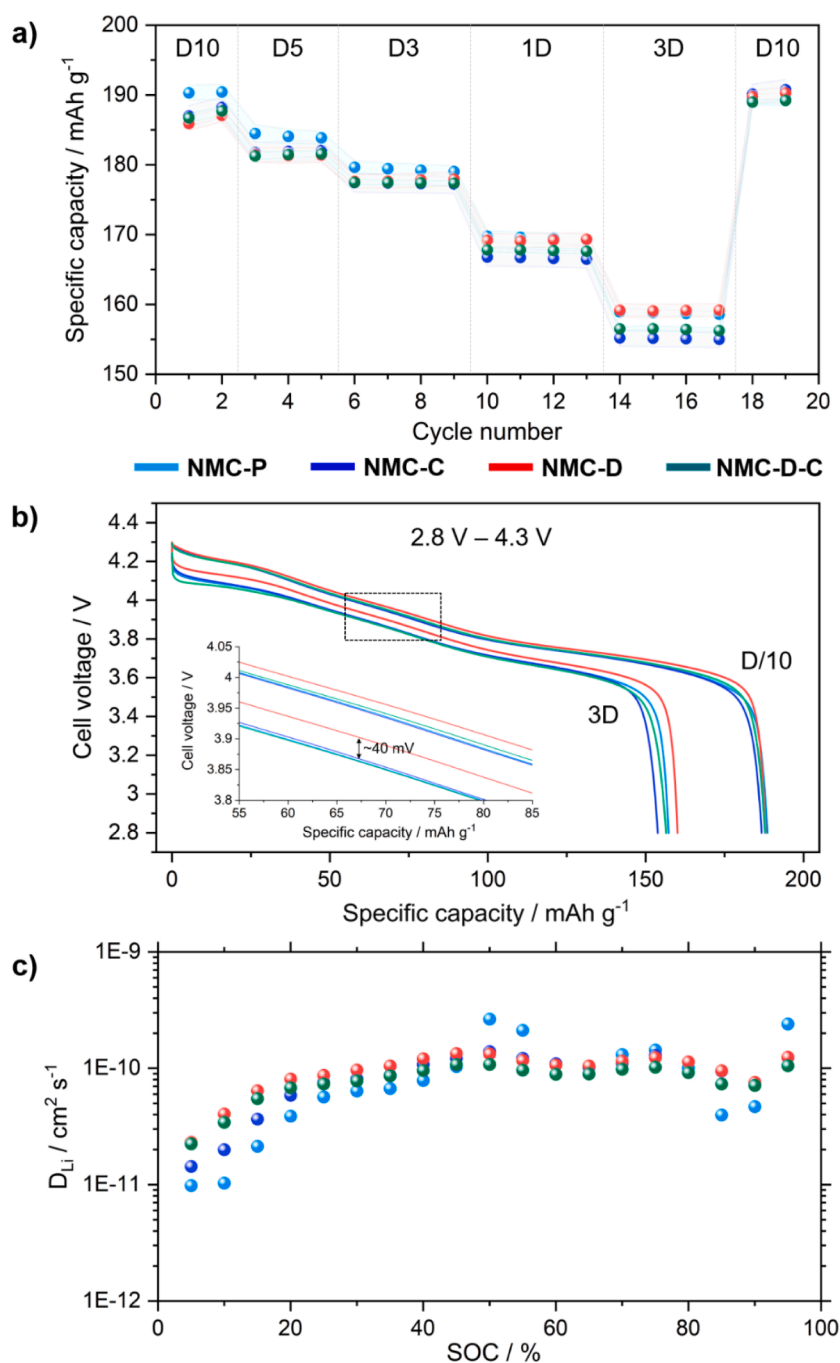


Fig. 3. Rate tests in half-cell configuration. The cells were cycled between 2.8 and 4.3 V and the charge rate was set to C/5 with the exception of two formation cycles at C/10, while the discharge rate was modified. a) Discharge capacity vs. cycle number, b) discharge voltage vs. specific capacity for the last cycles at D/10 and 3D, c) lithium diffusion coefficients vs. state-of-charge (SOC) determined via the GITT method. All experiments were carried at 25 °C. The typical mass loading of the positive electrodes was 4 mg/cm².

diffusion.

We further employed the galvanostatic intermittent titration technique (GITT) to determine the apparent diffusion coefficient of lithium as a function of the state of charge (SOC) for the different samples (Fig. 3c). We observed that during charge NMC-P has the lowest diffusion coefficient up to an SOC of 40%. The difference between NMC-P and NMC-D is particularly pronounced in the SOC range of 0–30%. For this range, we found ca. four times larger lithium diffusion coefficients for NMC-D compared to NMC-P. A larger diffusion coefficient in the low potential region is expected to be particularly beneficial at high charging rates. At SOC's larger than 50%, the difference in the lithium diffusion coefficient between the materials becomes negligible.

Constant current cycling data for Li/NMC half cells charged to 4.3 V is reported in Fig. 4a. The cells were charged at C/3 and discharged at 1C, conditions that are beneficial to the stability of the lithium metal counter electrode [27]. When the cut-off voltage is set to 4.3 V, the initial specific discharge capacity decreases in the order of $\text{NMC-P} > \text{NMC-D-C} > \text{NMC-D} > \text{NMC-C}$. We recorded a 1st cycle Coulombic efficiency of 85.0% for the pristine material (NMC-P). As expected, coating the material with titanium oxide increases the 1st cycle

efficiency to 85.6% and 85.4% for samples NMC-C and NMC-D-C, respectively. In contrast, doping the NMC811 with titanium decreases the 1st cycle efficiency to 83.7%. We ascribe the improved Coulombic efficiency to the low electronic conductivity of the titanium oxide coating layer that suppresses parasitic reactions such as electrolyte oxidation on the surface of the cathode material. The lower 1st cycle efficiency for the doped sample (NMC-D) might be related to the increased Ni/Li mixing vs. the pristine material (see again Table 2). Regarding cycling stability, NMC-P undergoes a slight capacity fading from the start which is absent for the titanium-modified samples. NMC-C displays a very constant capacity during 100 cycles. NMC-D and NMC-D-C display a significant capacity increase of 10 and 7 mAh/g during the first 50 cycles, respectively. This increase in capacity correlates with the amount of titanium used in the doping step performed at 750 °C: A lower amount of titanium was used for the first modification of sample NMC-D-C (0.3 mol%) compared to sample NMC-D (0.6 mol%).

Comparing the voltage profiles of NMC-P and NMC-D (Fig. 1b and 1d, respectively) also sheds light on the effect of cycling on the structural evolution of these samples. In the case of NMC-P, the slope of the voltage profile slightly increases after hundred cycles (Table 3). This is not

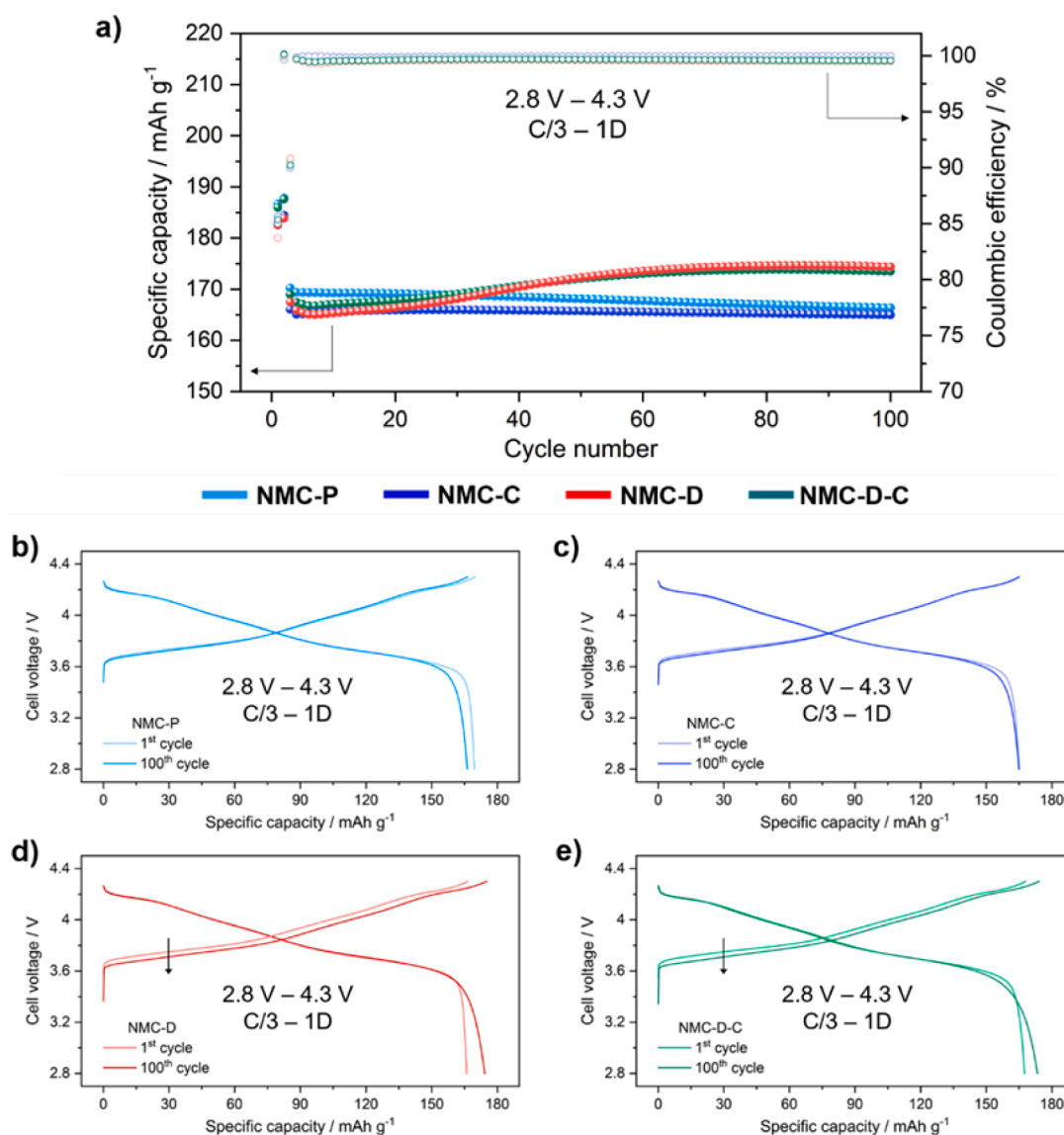


Fig. 4. Constant current cycling in half-cell configuration with a charge rate of C/3 and a discharge rate of 1D. The cells were cycled between 2.8 and 4.3 V. a) Discharge capacity and Coulombic efficiency vs. cycle number. b–e) Voltage profiles (cell voltage vs. specific capacity) of the 1st and 100th cycle for b) NMC-P, c) NMC-C, d) NMC-D, and e) NMC-D-C. The cells were initially subjected to two formation cycles at C/10. All experiments were carried out at 25 °C.

Table 3

Slope and average voltage of the 1st and 100th charge performed at C/3. The measurements were performed in half-cell configuration at 25 °C (see caption of Figure 4 for further details).

Sample	Slope of 1 st charge [mVg/mAh]	Slope of 100 th charge [mVg/mAh]	Average voltage 1 st charge [V]	Average voltage 100 th charge [V]
NMC-P	3.88	4.05	3.930	3.924
NMC-C	3.92	4.05	3.927	3.920
NMC-D	3.87	3.93	3.938	3.896
NMC-D-C	3.77	3.90	3.931	3.897

surprising as continuous charge and discharge (CCD) is indeed expected to increase the surface structural disorder [3]. The magnitude of this change is however small in line with the limited reduction in capacity. The picture is different for NMC-D, which instead displays a reduction in overpotential of 30 mV during charge from the first until the hundredth cycle. This finding points to a reduction in structural disorder, which is known to affect lithium diffusion in NMC [28,29].

Additional long-term cycling was conducted in full-cell configuration using graphite as anode material. The use of full cells avoids negative effects on cycling stability associated with lithium metal anodes and allows the use of cathodes with a higher and more realistic mass loading of in our case ca. 13 mg/cm² [30]. The discharge capacities as a function of cycle number of full cells charged to 4.2 and 4.4 V are shown in Fig. 5a and b, respectively. The cut-off voltage of 4.2 V was chosen as it is the most common upper cut-off voltage for graphite/NMC cells. To compensate for the ca. 0.1 V more negative redox potential of lithium, half cells were cycled to a cut-off voltage of 4.3 V. The cut-off voltage of 4.4 V was chosen as a reasonable compromise between increased capacity of the cathode material and impact on cycling stability. In line with the half-cell data, already the pristine NMC811 material (NMC-P) displays very good stability during cycling up to 4.2 V. Its capacity only

slightly declines from an initial value of 178 to 174 mAh/g after 200 cycles. A significant portion of the reduction in capacity for NMC-P occurs during the first 40 cycles, which is attributed to the higher reactivity of the unprotected surface compared to the modified materials.

Importantly, all modified samples display even better cycling stability. Contrary to NMC-P, NMC-C displays almost constant capacity during the first 40 cycles and subsequently displays only a very low rate of capacity fading, bringing the specific capacity after 200 cycles to 176 mAh/g from an initial value of 178 mAh/g. NMC-D, the doped material, shows instead a lower initial capacity of 170 mAh/g, in line with the results of the half-cell experiments. Upon cycling, the capacity recovers reaching a plateau value of 175 mAh/g after about 40 cycles. In the following cycles, the capacity is very stable with only minor degradation.

To better understand the origin of the initial capacity recovery for NMC-D, we performed Rietveld refinement analysis of X-ray diffraction patterns recorded on powders retrieved from electrodes after 50 cycles at C/3-D/3 (Fig. S9 and Table S2). Due to the little amount of powder available, only the spinning capillary configuration could be employed, leading to lower data quality and larger errors in the fit. In order to improve comparability, samples made from freshly prepared electrodes were analyzed in the same way. When comparing the change in the intensity ratios of the (003) and (104) reflections and the degree of Ni/Li mixing between the fresh and cycled electrodes, we find the largest reduction for sample NMC-D, in line with the pronounced increase in capacity seen in Fig. 5a for this material. However, further investigations are needed to understand why the degree of Ni/Li mixing decreases as no change in the degree of Ni/Li disorder has been reported for an NMC811 material after 1000 cycles at C/2 at room temperature in a potential range of 3.0 to 4.5 V vs. Li/Li⁺ [3].

Sample NMC-D-C shows again very promising cycling behavior. In an attempt to compensate for the initial capacity offset observed for NMC-D, we reduced the amount of titanium added during the doping

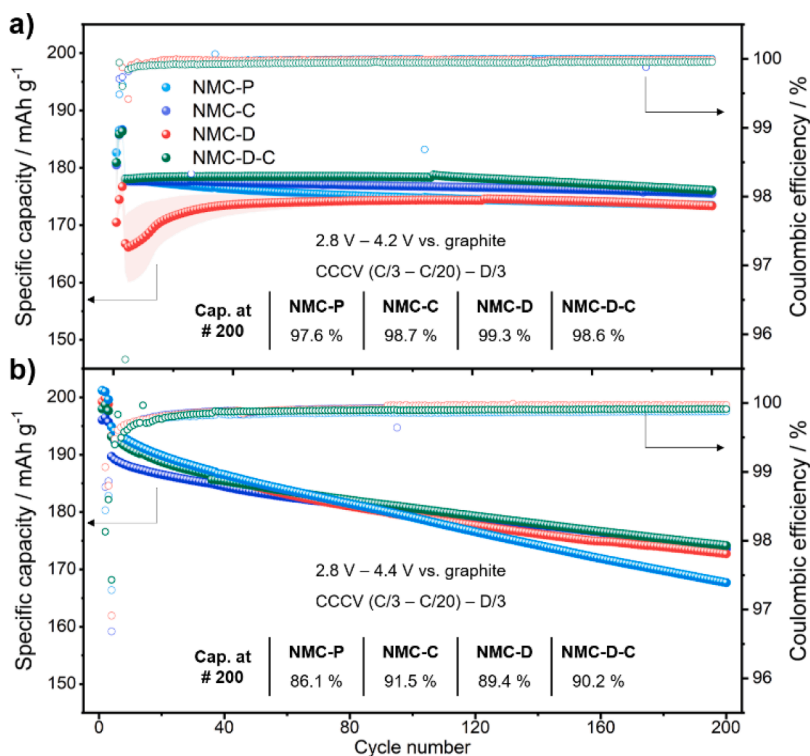


Fig. 5. Constant current-constant voltage cycling of graphite/NMC811 full cells. Specific capacity vs. cycle number plots of cells cycled in the voltage range of a) 2.8 – 4.2 V and b) 2.8 – 4.4 V. The cells were subjected to three formation cycles at C/10-D/10 followed by cycling at C/3-D/3. The constant voltage step was limited to a rate of C/20.

step at 750 °C from 0.6 mol% to 0.3 mol% as mentioned before. As expected, the specific capacity undergoes only a negligible recovery during the first cycles compared to NMC-D due to structural reordering, which is reflected in only minor changes in the (003)/(104) ratio and the degree of Ni/Li mixing during the first 50 cycles (see again Table S2). Importantly, we find no deficit in capacity with respect to NMC-P for NMC-D-C. The cycling stability of NMC-D-C is also further improved compared to NMC-C and NMC-D. Hence, NMC-D-C combines the benefits of doping and coating on cycling stability while avoiding the initial capacity penalty of NMC-D.

Based on the promising results observed for a cut-off voltage of 4.2 V, we decided to study the cycling stability at a higher cut-off voltage of 4.4 V. At this cut-off voltage, NMC-P displays the highest initial discharge capacity at C/10 of 201 mAh/g followed by the doped samples, i.e., NMC-D and NMC-D-C. NMC-C displays the lowest initial discharge capacity of 195 mAh/g. At 4.4 V, the fading of the pristine material (NMC-P) is initially similar to that of the Ti-doped samples. However, while the capacity fading rate gradually improves for the modified materials, NMC-P maintains the same fading rate, for a capacity retention of 86.1% after 200 cycles. All modified materials show better capacity retention after 200 cycles: It increases from 89.4% for NMD-D over 90.2% for NMC-D-C to 91.5% for NMC-C, hinting at a beneficial effect of the more inert TiO₂ layer towards electrolyte decomposition.

For the cut-off voltage of 4.4 V, the fading rate is significantly accelerated compared to 4.2 V, enhancing the differences between pristine and modified NMC materials. However, cycling NMC811 above 4.2 V is known to affect the stability of the material itself provoking increased cracking of the NMC particles due to the more pronounced lattice volume changes [1,31]. To investigate the effect of the titanium modification without exposing the materials to excessively high voltages and to disentangle oxidative stability from cracking, we employed an accelerated aging test (AAT) where the electrodes were repeatedly exposed to 4.2 V vs. graphite for 10 h followed by one full recovery cycle to probe the capacity of the electrode (see Fig. S3 for an illustration of the employed AAT cycling protocol). This protocol minimizes rapid lattice volume changes at high voltage and allows focusing specifically on electrolyte decomposition [1,32]. For a typical CCCV cycle at C/3, the time spent at 4.2 V is ca. 10 min, whereas for our AAT experiment it is more than 10 h. Therefore, one voltage-hold step of this AAT corresponds to roughly 60 cycles in terms of time spent at high voltage.

As expected, this AAT is significantly more demanding in terms of oxidative stability than the conventional CCCV cycling to 4.2 V discussed above. The pristine (NMC-P) and coated material (NMC-C) behave similarly under these conditions, with respectively 160 and 170 h at 4.2 V required to reach 90% of the initial capacity (see Fig. 6a). In contrast, both doped NMC-D and NMC-D-C require longer exposure to high voltage to lose 10% of the initial capacity, i.e., 200 and 260 h,

respectively. As shown in Fig. 6b, this difference primarily arises from the first ten voltage hold steps where NMC-D-C is significantly more stable than the other materials. Afterwards all materials display a similar fading rate. The better capacity retention of NMD-D-C during the first 100 h at 4.2 V is also reflected in a higher cumulative Coulombic efficiency (CCE), see experimental section for definition, during most of the first ten steps compared to the other materials (see again Fig. 6a). Hence, combining doping and coating seems to have clear advantages during voltage hold at 4.2 V.

As shown in the SEM images in Fig. 7a and 7c, fresh NMC-P and NMC-D-C display secondary particles that are dense, with only a few voids in the center. After the AAT, widespread cracks are easily visible in the cross section of the NMC-P particle. In contrast, cycled NMC-D-C particles display significantly fewer and smaller cracks (Fig. 7d), in line with the better capacity retention and higher CCE of NMC-D-C compared to NMC-P.

We conclude that the simultaneous presence of TiO₂ on the surface and of titanium in the bulk effectively suppresses direct contact between the electrolyte and the primary particles of the active material and increases the resilience of the material against volume changes, respectively. Combined, these protection strategies significantly enhance the cycling and high-voltage stability of NMC811.

As doping and coating are performed in two separate steps, we expect that the stability of Ni-rich NMC can be further improved by combining different modification elements that have specific advantages for either bulk or interface stability. For example, both aluminum and tungsten are known to effectively stabilize the bulk structure of NMC [33,34], while other elements might be more suitable to form coatings.

4. Conclusion

In conclusion, we showed that titanium can be used to modify NMC811 towards enhanced cycling stability. The choice of annealing conditions allows localizing titanium on the surface as a thin TiO₂ layer or incorporating titanium as dopant inside the bulk of the material.

The electrochemical performance of NMC811 is strongly affected by the chosen approach. A TiO₂ coating suppresses the initial capacity fading that occurs for pristine NMC811 upon cycling. However, its presence slightly reduces the rate performance and does not provide significant protection when the material is held at high voltages for an extended period of time, possibly due to fracturing of the coating as a result of volume changes and subsequent exposure of bare NMC811 surface.

At higher calcination temperatures, titanium diffuses into the bulk of the NMC particles, leading to unit cell expansion and Li/Ni exchange. The former improves the rate performance, while the later lowers the

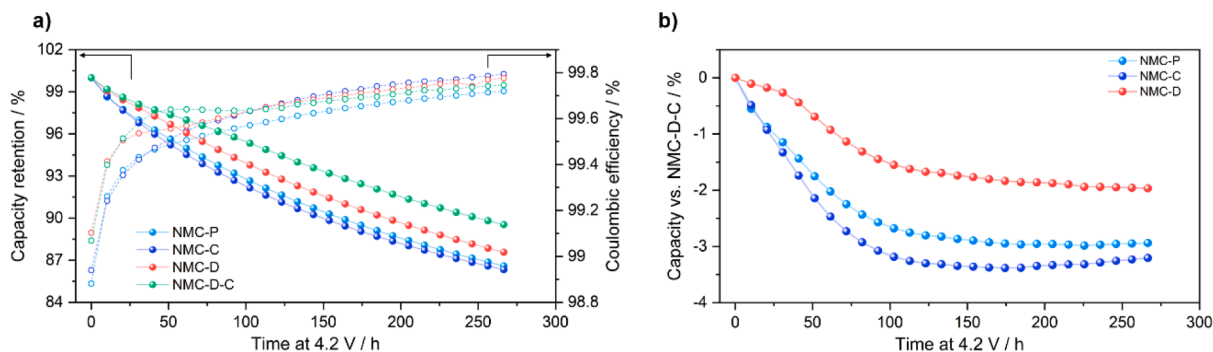


Fig. 6. Cycling of graphite/NMC811 full cells with voltage hold steps of 10 h at 4.2 V. a) Capacity retention and cumulative Coulombic efficiency (CCE, see experimental section for definition) and b) capacity retention of NMC-P, NMC-C, and NMC-D relative to NMC-D-C, the best-performing material using these cycling conditions. The cells were cycled between 2.8 and 4.2 V at C/3 and held at the upper cut-off voltage of 4.2 V for 10 h every second cycle (see experimental section for further details). All experiments were carried out at 25 °C.

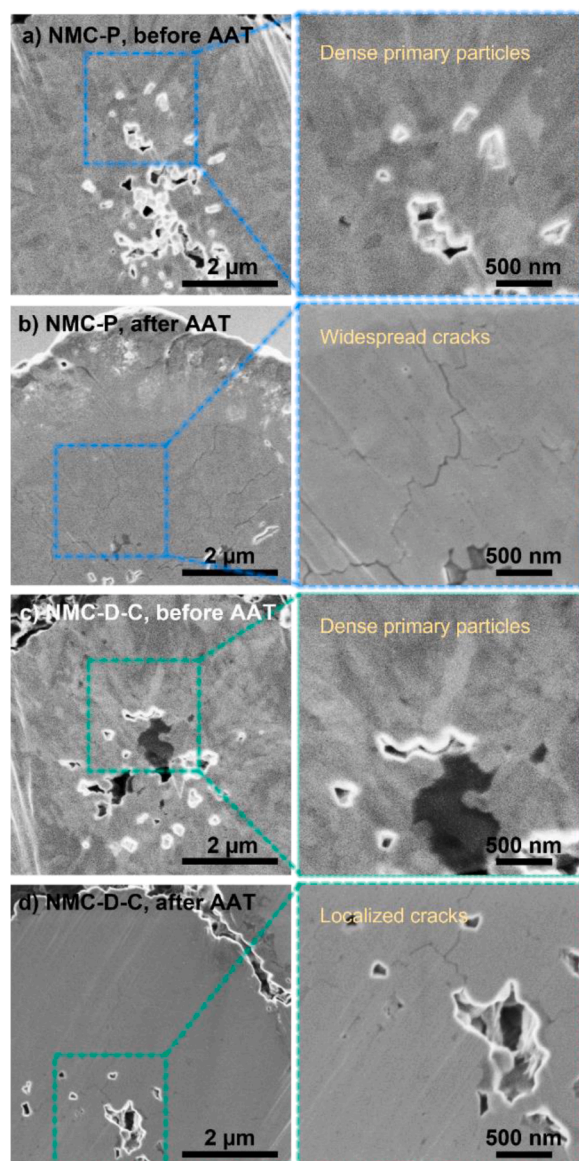


Fig. 7. SEM images of cross sections of freshly prepared a) NMC-P and c) NMC-D-C electrodes and of b) NMC-P and d) NMC-D-C electrodes recovered after the accelerated aging test (see Fig. 6).

initial discharge capacity. In addition, this modification improves the cycling stability of NMC811, particularly at high voltage.

Importantly, the drawbacks of the two individual modifications can be overcoming by combining both in a two-step modification while maintaining their benefits. When combining a TiO_2 layer on the surface with titanium in the bulk, we observe high cycling stability and high capacity both during cycling to cut-off voltages of 4.2 V and 4.4 V (in full cells vs. graphite) as well as during voltage-hold experiments. As doping and coating are performed in two separate steps, we expect that the stability of NMC811 can be further improved by combining different modification elements, e.g., Ti, Al, W, etc., that have specific advantages for either bulk or interface stability.

CRedit authorship contribution statement

Francesco Bizzotto: Conceptualization, Methodology, Investigation, Writing – original draft, Writing – review & editing. **Walid Dachraoui:** Investigation. **Rabeb Grissa:** Investigation. **Wengao Zhao:** Investigation. **Francesco Pagani:** Investigation. **Edouard Querel:**

Investigation. **Ruben-Simon Kühnel:** Funding acquisition, Conceptualization, Methodology, Supervision, Writing – review & editing. **Corsin Battaglia:** Funding acquisition, Conceptualization, Supervision, Writing – review & editing.

Declaration of Competing Interest

The authors declare that they have no known competing financial interests or personal relationships that could have appeared to influence the work reported in this paper.

Data availability

Data will be made available on request.

Acknowledgments

The authors thank the European Union for funding this work through the project “SeNSE”: This project has received funding from the European Union’s Horizon 2020 research and innovation program under grant agreement No 875548. The authors thank Solvionic and the MEET Battery Research Center at the University of Münster, Germany, for providing the electrolyte and the graphite electrodes, respectively.

Supplementary materials

Supplementary material associated with this article can be found, in the online version, at [doi:10.1016/j.electacta.2023.142758](https://doi.org/10.1016/j.electacta.2023.142758).

References

- [1] A.O. Kondrakov, A. Schmidt, J. Xu, H. Geßwein, R. Mönig, P. Hartmann, H. Sommer, T. Brezesinski, J. Janek, Anisotropic lattice strain and mechanical degradation of high- and low-nickel NCM cathode materials for Li-Ion batteries, *J. Phys. Chem. C* 121 (2017) 3286–3294.
- [2] Z. Xu, M.M. Rahman, L. Mu, Y. Liu, F. Lin, Chemomechanical behaviors of layered cathode materials in alkali metal ion batteries, *J. Mater. Chem. A* 6 (2018) 21859–21884.
- [3] F. Friedrich, B. Strehle, A.T.S. Freiberg, K. Kleiner, S.J. Day, C. Erk, M. Piana, H. A. Gasteiger, Capacity Fading Mechanisms of NCM-811 Cathodes in Lithium-Ion Batteries Studied by X-ray Diffraction and Other Diagnostics, *J. Electrochem. Soc.* 166 (2019) A3760–A3774.
- [4] L. Zhang, E.A. Müller Gubler, C.-W. Tai, L. Kondracki, H. Sommer, P. Novák, M. El Kazzi, S. Trabesinger, Elucidating the humidity-induced degradation of Ni-rich layered cathodes for Li-ion batteries, *ACS Appl. Mater. Interfaces* 14 (2022) 13240–13249.
- [5] Y. Kim, H. Park, J.H. Warner, A. Manthiram, Unraveling the Intricacies of Residual Lithium in High-Ni Cathodes for Lithium-Ion Batteries, *ACS Energy Lett.* 6 (2021) 941–948.
- [6] H.H. Sun, H.H. Ryu, U.H. Kim, J.A. Weeks, A. Heller, Y.K. Sun, C.B. Mullins, Beyond doping and coating: prospective strategies for stable high-capacity layered Ni-rich cathodes, *ACS Energy Lett.* 5 (2020) 1136–1146.
- [7] A. Manthiram, J.C. Knight, S.T. Myung, S.M. Oh, Y.K. Sun, Nickel-rich and lithium-rich layered oxide cathodes: progress and perspectives, *Adv. Energy Mater.* 6 (2016), 1501010.
- [8] H. Darjazi, E. Gonzalo, B. Acebedo, R. Cid, M. Zarrabeitia, F. Bonilla, M.A. Muñoz-Márquez, F. Nobili, Improving high-voltage cycling performance of nickel-rich NMC layered oxide cathodes for rechargeable lithium-ion batteries by Mg and Zr co-doping, *Mater. Today Sustain.* 20 (2022), 100236.
- [9] Y. Deng, J. Mou, H. Wu, N. Jiang, Q. Zheng, K.H. Lam, C. Xu, D. Lin, A superior Li_2SiO_3 -composited $\text{LiNi}_{0.5}\text{Mn}_{1.5}\text{O}_4$ cathode for high-voltage and high-performance lithium-ion batteries, *Electrochim. Acta* 235 (2017) 19–31.
- [10] B. Song, W. Li, S.-M. Oh, A. Manthiram, Long-life nickel-rich layered oxide cathodes with a uniform Li_2ZrO_3 surface coating for lithium-ion batteries, *ACS Appl. Mater. Interfaces* 9 (2017) 9718–9725.
- [11] F. Xin, H. Zhou, X. Chen, M. Zuba, N. Chernova, G. Zhou, M.S. Whittingham, Li–Nb–O coating/substitution enhances the electrochemical performance of the $\text{LiNi}_{0.8}\text{Mn}_{0.1}\text{Co}_{0.1}\text{O}_2$ (NMC 811) cathode, *ACS Appl. Mater. Interfaces* 11 (2019) 34889–34894.
- [12] P. Karayaylali, R. Tatara, Y. Zhang, K.-L. Chan, Y. Yu, L. Giordano, F. Maglia, R. Jung, I. Lund, Y. Shao-Horn, Coating-dependent electrode-electrolyte interface for Ni-rich positive electrodes in Li-ion batteries, *J. Electrochem. Soc.* 166 (2019) A1022–A1030.

- [13] B. Han, B. Key, A.S. Lipton, J.T. Vaughey, B. Hughes, J. Trevey, F. Dogan, Influence of coating protocols on alumina-coated cathode material: atomic layer deposition versus wet-chemical coating, *J. Electrochem. Soc.* 166 (2019) A3679–A3684.
- [14] Q. Gan, N. Qin, Z. Wang, Z. Li, Y. Zhu, Y. Li, S. Gu, H. Yuan, W. Luo, L. Lu, Z. Xu, Z. Lu, Revealing mechanism of Li_3PO_4 coating suppressed surface oxygen release for commercial Ni-rich layered cathodes, *ACS Appl. Energy Mater.* 3 (2020) 7445–7455.
- [15] Q. Fan, K. Lin, S. Yang, S. Guan, J. Chen, S. Feng, J. Liu, L. Liu, J. Li, Z. Shi, Constructing effective TiO_2 nano-coating for high-voltage Ni-rich cathode materials for lithium ion batteries by precise kinetic control, *J. Power Sources* 477 (2020), 228745.
- [16] W. Wang, L. Wu, Z. Li, K. Huang, J. Jiang, Z. Chen, X. Qi, H. Dou, X. Zhang, *In situ* tuning residual lithium compounds and constructing TiO_2 coating for surface modification of a nickel-rich cathode toward high-energy lithium-ion batteries, *ACS Appl. Energy Mater.* 3 (2020) 12423–12432.
- [17] X. Fan, X. Ou, W. Zhao, Y. Liu, B. Zhang, J. Zhang, L. Zou, L. Seidl, Y. Li, G. Hu, C. Battaglia, Y. Yang, *In situ* inorganic conductive network formation in high-voltage single-crystal Ni-rich cathodes, *Nat. Commun.* 12 (2021) 5320.
- [18] A. Nickol, T. Schied, C. Heubner, M. Schneider, A. Michaelis, M. Bobeth, G. Cuniberti, GITT analysis of lithium insertion cathodes for determining the lithium diffusion coefficient at low temperature: challenges and pitfalls, *J. Electrochem. Soc.* 167 (2020), 090546.
- [19] C. Xu, P.J. Reeves, Q. Jacquet, C.P. Grey, Phase behavior during electrochemical cycling of Ni-rich cathode materials for Li-ion batteries, *Adv. Energy Mater.* 11 (2021), 2003404.
- [20] W. Cho, J.H. Song, K.W. Lee, M.W. Lee, H. Kim, J.S. Yu, Y.J. Kim, K.J. Kim, Improved particle hardness of Ti-doped $\text{LiNi}_{1/3}\text{Co}_{1/3}\text{Mn}_{1/3}\text{Ti}_x\text{O}_2$ as high-voltage cathode material for lithium-ion batteries, *J. Phys. Chem. Solids* 123 (2018) 271–278.
- [21] T. Wang, K. Ren, W. Xiao, W. Dong, H. Qiao, A. Duan, H. Pan, Y. Yang, H. Wang, Tuning the Li/Ni disorder of the NMC811 cathode by thermally driven competition between lattice ordering and structure decomposition, *J. Phys. Chem. C* 124 (2020) 5600–5607.
- [22] S.M. Bak, E. Hu, Y. Zhou, X. Yu, S.D. Senanayake, S.J. Cho, K.B. Kim, K.Y. Chung, X.Q. Yang, K.W. Nam, Structural changes and thermal stability of charged $\text{LiNi}_x\text{Mn}_y\text{Co}_z\text{O}_2$ cathode materials studied by combined *in situ* time-resolved XRD and mass spectroscopy, *ACS Appl. Mater. Interfaces* 6 (2014) 22594–22601.
- [23] W. Liu, P. Oh, X. Liu, M.-J. Lee, W. Cho, S. Chae, Y. Kim, J. Cho, Nickel-rich layered lithium transition-metal oxide for high-energy lithium-ion batteries, *Angew. Chem. Int. Ed.* 54 (2015) 4440–4457.
- [24] F. Schipper, E.M. Erickson, C. Erk, J.Y. Shin, F.F. Chesneau, D. Aurbach, Recent advances and remaining challenges for lithium ion battery cathodes, *J. Electrochem. Soc.* 164 (2017) A6220–A6228.
- [25] K. Kang, G. Ceder, Factors that affect Li mobility in layered lithium transition metal oxides, *Phys. Rev. B* 74 (2006), 094105.
- [26] W. Yan, S. Yang, Y. Huang, Y. Yang, G. Yuan, A review on doping/coating of nickel-rich cathode materials for lithium-ion batteries, *J. Alloy. Compd.* 819 (2020), 153048.
- [27] A.J. Louli, M. Coon, M. Genovese, J. deGooyer, A. Eldesoky, J.R. Dahn, Optimizing cycling conditions for anode-free lithium metal cells, *J. Electrochem. Soc.* 168 (2021), 020515.
- [28] S.B. Schougaard, J. Bréger, M. Jiang, C.P. Grey, J.B. Goodenough, $\text{LiNi}_{0.5}\text{Mn}_{0.5}\text{O}_2$ —a high-rate, high-capacity cathode for lithium rechargeable batteries, *Adv. Mater.* 18 (2006) 905–909.
- [29] E. Zhao, L. Fang, M. Chen, D. Chen, Q. Huang, Z. Hu, Q.-b. Yan, M. Wu, X. Xiao, New insight into Li/Ni disorder in layered cathode materials for lithium ion batteries: a joint study of neutron diffraction, electrochemical kinetic analysis and first-principles calculations, *J. Mater. Chem. A* 5 (2017) 1679–1686.
- [30] R. Nölle, K. Beltrop, F. Holtstiege, J. Kasnatscheew, T. Placke, M. Winter, A reality check and tutorial on electrochemical characterization of battery cell materials: How to choose the appropriate cell setup, *Mater. Today* 32 (2020) 131–146.
- [31] N. Laszczynski, S. Solchenbach, H.A. Gasteiger, B.L. Lucht, Understanding electrolyte decomposition of graphite/NCM811 cells at elevated operating voltage, *J. Electrochem. Soc.* 166 (2019) A1853–A1859.
- [32] H.-H. Ryu, B. Namkoong, J.H. Kim, I. Belharouak, C.S. Yoon, Y.K. Sun, Capacity fading mechanisms in Ni-rich single-crystal NCM cathodes, *ACS Energy Lett.* 6 (2021) 2726–2734.
- [33] U.H. Kim, N.Y. Park, G.T. Park, H. Kim, C.S. Yoon, Y.K. Sun, High-energy W-doped $\text{Li}[\text{Ni}_{0.95}\text{Co}_{0.04}\text{Al}_{0.01}]\text{O}_2$ cathodes for next-generation electric vehicles, *Energy Stor. Mater.* 33 (2020) 399–407.
- [34] K. Zhou, Q. Xie, B. Li, A. Manthiram, An in-depth understanding of the effect of aluminum doping in high-nickel cathodes for lithium-ion batteries, *Energy Storage Mater.* 34 (2021) 229–240.